

Extrinsic Chirality and Circular Dichroism at Visible Frequencies Enabled by Birefringent α -MoO₃ Nanoscale-Thick Films: Implications for Chiro-Optical Control

Emilija Petronijevic,* Sina Abedini Dereshgi, Maria Cristina Larciprete, Marco Centini, Concita Sibilia, and Koray Aydin*



Cite This: *ACS Appl. Nano Mater.* 2022, 5, 5609–5616



Read Online

ACCESS |



Metrics & More



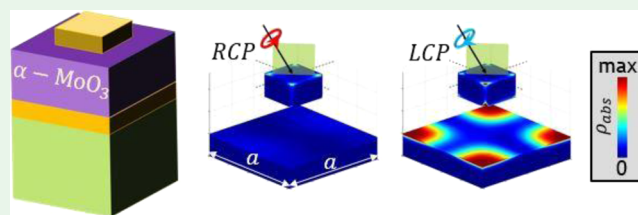
Article Recommendations



Supporting Information

ABSTRACT: Nanophotonics community has shown great interest in 2D materials because of their unique properties of electromagnetic field manipulation. Many of these materials exhibit strong natural anisotropy, which further opens possibilities of polarization manipulation. Here, we show that α -MoO₃, an emerging natural hyperbolic 2D material, can be combined with plasmonic nanostructures to provide strong extrinsic chirality in the visible range. A combination of biaxial anisotropy in α -MoO₃ and Fabry–Perot cavities with nanoscale features leads to different absorption of left and right circularly polarized photons, hence exhibiting circular dichroism (CD). Our simulation results predict that multilayer nanoscale-thick films including α -MoO₃ are potential candidates for achieving extrinsic chirality across the visible range. Furthermore, we show a significant CD increase when the α -MoO₃ layer is coupled with plasmonic nanohole arrays or plasmonic nanocubes. Such designs are achiral in geometry and therefore easier to fabricate. Moreover, we optimize the CD dissymmetry factor g_{CD} for the nanocube-based design at 780 nm, obtaining 84%. We believe that utilizing biaxially anisotropic α -MoO₃ films to control and engineer chiro-optical properties in the visible frequency range will open research directions and enable enhanced functionalities in chiro-optical control at the nanoscale, further leading to applications in chiral sensing and CD.

KEYWORDS: α -MoO₃, MIM, extrinsic chirality, circular dichroism plasmonics, metamaterial



1. INTRODUCTION

Chirality, a lack of mirror symmetry, is a common property of our world that comes in all dimensions. At the molecular level, a chiral molecule cannot be superimposed on its mirror image. Like our hands, there are left and right version of a chiral molecule, called enantiomers. Although the two enantiomers are equal in atomic composition, they can have different biological activity and toxicity; for example, in chiral drugs, while one enantiomer acts as a drug, the other one can remain inactive or even lead to serious side effects.^{1,2} Chirality of a chiral solution is detected via its differential absorption for circular polarizations of opposite handedness, that is, circular dichroism (CD). However, intrinsic CD of chiral molecules is usually extremely low, which aggravates the detection of ultralow concentrations of “bad” enantiomers.

Owing to the development of nanotechnology, we can nowadays artificially design novel materials, which exhibit high CD signals. Led by the exotic features of materials at the nanoscale, photonics community has, in fact, proposed plasmonic,^{3–10} dielectric,^{11–13} and hybrid^{14–18} nanostructures with high intrinsic chirality in the visible range. Recent experimental studies prove that dielectric and plasmonic periodically arranged nanostructures can improve chiral

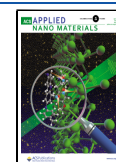
sensing of specific enantiomers.^{19,20} Moreover, even if the nanostructure is not intrinsically chiral, the symmetry of the light–matter interaction can be broken with an experimental setup.²¹ This so-called extrinsic chirality is a property of various achiral nanostructures periodically organized in metamaterials and properly tilted at oblique incidence.^{22–26} Therefore, we can avoid complex fabrication of intrinsical chiral shapes of nanoscale features by inducing the asymmetry between the metamaterial and the incoming circularly polarized light.

The fabrication cost of future chiral nanosensors can be lowered by using self-assembling approaches for extrinsic chirality. Nanosphere lithography or self-assembled nanowire growth can be combined with tilted plasmonic deposition to obtain high-quality samples, which exhibit extrinsic chirality.^{27–35} Moreover, we could even completely avoid the

Received: February 7, 2022

Accepted: March 28, 2022

Published: April 11, 2022



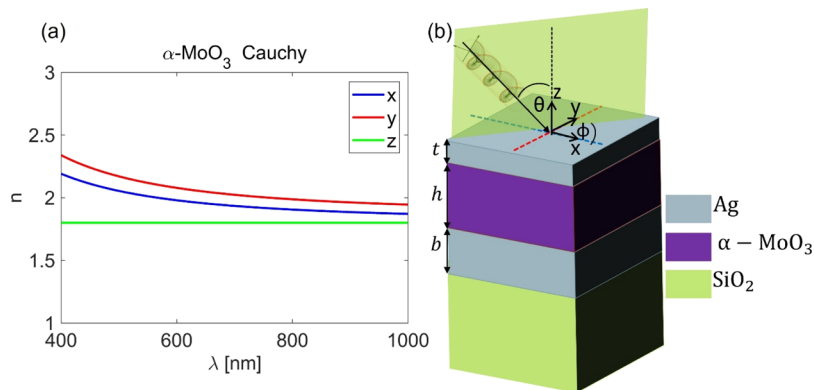


Figure 1. (a) Refractive index of α -MoO₃ in the 400–1000 nm range in all three directions. (b) Schematic of the investigated MIM structure, where the green plane defines the oblique excitation at θ , tilted in the xy -plane for ϕ .

nanofabrication processes if we consider chirality in naturally hyperbolic media, such as van der Waals materials. One such example is a bilayer structure of twisted hexagonal boron nitride (hBN) slabs;³⁶ even though hBN lacks in-plane anisotropy, the twist between the two layers leads to a difference in transmission of left and right circular polarizations (LCP and RCP, respectively). The transmission difference was optimized to 0.84 in the infrared range; however, experimental realization of this numerical proposal would be complicated because of the definition of the precise tilt angle between the layers. Another interesting material is black phosphorus (BP), which does support a slight in-plane anisotropy.³⁷ Authors in ref 38 show that a simple geometry of the BP monolayer on glass can provide extrinsic chiral effects in transmission; however, these effects are weak and require large oblique incidence angles. Another very recent work proposes the structured square nanopatch arrays of BP for dynamic chirality control in the THz regime.³⁹ Significantly large extrinsic chiral effects can be expected in the naturally hyperbolic biaxial material α -phase molybdenum trioxide (α -MoO₃), which exhibits high anisotropy;^{40,41} indeed, authors in ref 42 report on the strong extrinsic chiral behavior of α -MoO₃ films of micrometer thickness. The last work naturally treats CD in the long infrared wavelength range, where the permittivity of α -MoO₃ exhibits strong hyperbolic biaxial features. However, with current growth techniques, it is difficult to obtain films of micrometer thicknesses. Useful applications of chirality with visible light and thinner α -MoO₃ are still unexplored due to much lower anisotropy of α -MoO₃ in the visible range. Moreover, its combination with nanoscale structuring of plasmonic layers can enhance the electromagnetic confinement, thus leading to an increase in the effective anisotropy of light–matter interaction.

In this work, we explore the possibility to use α -MoO₃ anisotropy in the visible range for extrinsic chirality in metal–insulator–metal (MIM) structures with nanoscale features. Recent experimental work reported the polarization-sensitive behavior in metal– α -MoO₃–metal structures due to the polarization-dependent refractive index of this 2D material.⁴³ We start from a layered simple geometry and show how it can be extended for extrinsic chirality in the visible range. We investigate MIM based on Au or Ag; the bottom and top plasmonic layers are optically thick and thin, respectively. Absorption resonances at oblique incidence differ for LCP and RCP excitation, producing CD dissymmetry given by factor g_{CD} , which reaches as high as 27%. We further show that

simple achiral nanofabrication of the bottom plasmonic layer can drastically enhance g_{CD} in the visible range; for the nanohole-array (NHA) MIM structure, g_{CD} maximum is in the 50% range. Finally, we address the possibility of nanostructuring of the top plasmonic layer, which improves g_{CD} to around 84% at 780 nm. We believe that our designs can open novel functionalities of 2D materials for applications in chiro-optical control and manipulation in the visible range.

2. DESIGN AND NUMERICAL SETUP

In the following, we investigate electromagnetic confinement and resonant absorption in the MIM design with α -MoO₃ as a dielectric layer. We consider the visible and near-infrared range from 400 to 1000 nm. The n – k model of α -MoO₃ was extracted by conducting reflection/transmission measurements on α -MoO₃ flakes grown on a transparent quartz substrate. Because the loss is negligible for α -MoO₃ in the visible range, k is negligible and the Cauchy model is used to fit to the measured data (also available in ref 43). In Figure 1a, the refractive indices are plotted in all three directions. In Figure 1b, we sketch the MIM design and the excitation under which extrinsic chirality can be expected. A MIM structure lies on a glass substrate, and it is made of a bottom plasmonic layer, a middle α -MoO₃ layer, and a top plasmonic layer; these layers have b , h , and t thicknesses, respectively. We investigate this design by full-wave 3D electromagnetic simulations based on the finite-difference time domain (FDTD) commercially available solver by Lumerical.⁴⁴ The FDTD surrounds the MIM structure with Bloch boundary conditions in the xy -plane, and the perfectly matched layers (PMLs) in the z -direction; because we treat oblique incidence excitation for extrinsic chirality, we performed convergence testing to ensure simulation stability in terms of PML properties and distance from the structure. The refractive index of α -MoO₃ is imported as the anisotropic model given by data in Figure 1a, with correspondingly defined axes; Ag and Au complex permittivities are taken from the Lumerical database. The thickness of the bottom plasmonic layer is fixed at $b = 200$ nm.

We excite the MIM structure from the top with two perpendicular plane-wave sources; these sources are similar in all properties except for the phase difference of 90° (-90°), which simulates RCP (LCP) excitation. The type of these plane waves is called broadband fixed angle source technique, which is specifically dedicated to the oblique broadband excitation. The direction of the incident field is defined by the oblique angle θ and the azimuthal tilt angle ϕ ; the incidence

plane is indicated by the green transparent region in Figure 1b, where θ defines the angular offset of the wave vector with respect to the z -axis, while ϕ defines the offset of the incidence plane from the xz -plane.

CD is defined as a normalized differential absorption between LCP and RCP excitation, given by the CD dissymmetry factor g_{CD}

$$g_{\text{CD}} [\%] = 100 \cdot \frac{A_{\text{LCP}} - A_{\text{RCP}}}{A_{\text{LCP}} + A_{\text{RCP}}} \quad (1)$$

with A_{LCP} (A_{RCP}) being total absorbed power for LCP (RCP) excitation. The absorption density is calculated from 3D electric field and refractive index monitors as

$$\rho_{\text{abs}} = -0.5\omega^2 |\vec{E}|^2 \text{Im}\{\epsilon\} \quad (2)$$

and integrated over MIM to obtain total absorption. In the following, we investigate ρ_{abs} , g_{CD} , and electric field in the MIM structure. We investigate Ag and Au because their plasmonic properties differ in the high energy range, making design with Ag more suitable for the blue range and design with Au for near-infrared applications.

3. RESULTS AND DISCUSSION

3.1. Multilayer MIM Structure. *3.1.1. Linearly Polarized Excitation.* We start by considering a 400 nm-thick isotropic lossless dielectric material, which has a refractive index of 2 across the whole range (as an average index from Figure 1a); it is sandwiched between two Ag layers, with $b = 200$ nm and $t = 20$ nm. Such MIM exhibits Fabry–Perot (FP) resonances in the range of our interest, as shown in Figure 2; as expected

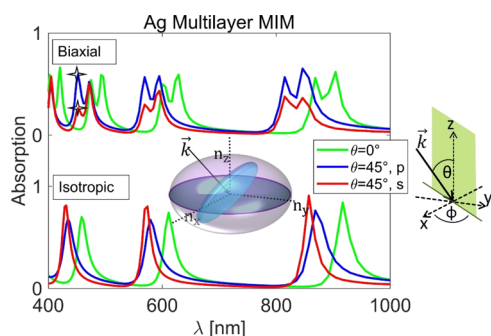


Figure 2. Absorption spectra for isotropic and biaxial (α - MoO_3) MIM structures, excited at normal and oblique incidence; geometric parameters are $b = 200$ nm, $h = 400$ nm, $t = 20$ nm, and $\phi = 45^\circ$; insets show the refractive index ellipsoid of α - MoO_3 and the visual schematic of the defined angles θ and ϕ .

from the z -projection of the light wave vector \vec{k} , the resonances blue-shift with the increase in the incidence angle. At an oblique incidence of 45° , p- and s-polarized light excite resonances, which slightly differ in strength and spectral position; this stems from the different reflection coefficient of the plasmonic layer.

We next change the insulator material to α - MoO_3 and note a more complex behavior due to the birefringence. In the inset of Figure 2, the ordinary and extraordinary refractive indices of this material strongly depend on the incident angles θ and ϕ . Even though the spectral position of the absorption peaks is centered similar to the isotropic case, the peaks split into two absorption maxima, which blue-shift at oblique incidence, as expected. This behavior can be understood in terms of the

effective refractive index of biaxial crystals, where each polarization of the incoming light interacts with different refractive index values for a non-zero θ and ϕ ; because these indices are different for the two polarizations, their absorption peaks appear at different wavelengths, given the constant thickness h . The MIM absorption dependence on the electric field direction of the linearly polarized light was already experimentally observed at normal incidence in ref 43. Even though the in-plane anisotropy of α - MoO_3 is rather low in the visible range, the resonant FP structure enhances this behavior, potentially leading to applications in transmission and reflection color filters. Oblique incidence offers an additional degree of freedom in terms of wavelength tuneability. Moreover, when combined with a biaxial structure, oblique incidence of circularly polarized light leads to chiro-optical processes, as it will be shown later.

Next, let us consider electromagnetic wave propagation in the α - MoO_3 -hybridized MIM at 452 nm, for $\theta = 45^\circ$ and $\phi = 45^\circ$. At this wavelength, p-polarized light is resonantly absorbed, while s-polarization induces much lower absorption (“stars” in Figure 2). In Figure S1, we visualize time evolution (across one optical cycle) of the near-field distribution for three electric field components, for the p- and s-polarized excitation. For the s-polarized excitation, there is an obvious higher reflection (hence lower absorption). Because circular polarization is a combination of properly dephased p and s polarizations, a phase shift of 90° (-90°) would produce a constructive (destructive) interference of the p and s polarizations in the air. Therefore, RCP (LCP) excitation would involve a constructive (destructive) interference of the p and s polarizations in the air, increasing (decreasing) the reflection and decreasing (increasing) the absorption.

3.1.2. Circularly Polarized Excitation. Previously presented interference of the electric fields under combined s- and p-polarized excitations is the required condition for the appearance of CD. In Figure 3a, we plot the absorption spectra for LCP and RCP excitations (all the other geometric parameters are the same as before). Indeed, we note that the destructive interference of s- and p-polarized excitations, dephased in time, leads to an absorption peak for the LCP wave at 452 nm. We next calculate g_{CD} (eq 1) for the MIM structure of previous dimensions, considering also Au as a plasmonic layer, Figure 4b. For Ag-based MIM, the larger absorption of LCP at 452 nm leads to the positive value of CD, which in this range reaches 18%. Au-based MIM of the same dimensions exhibits similar CD features, while it performs worse than Ag in the blue range due to its inherent loss. In the near-infrared range, the CD behavior is almost equal; this is expected because in this MIM design of constant parameters, parameters that define extrinsic chirality are θ , ϕ , and h .

We further prove the previous idea of interfering fields from dynamic simulations (Figure S2). We plot the distribution of the electric field intensity over the volume of the Ag-based MIM structure at 452 nm; Figure 3c shows the higher enhancement of the FP cavity antinodes for LCP excitation in the volumetric part of α - MoO_3 . Therefore, LCP absorption is enhanced compared to RCP. Au-based MIM shows opposite CD in the near-infrared range, reaching an absolute maximum of 27% at 846 nm. Corresponding electric field intensity is therefore much higher in the MIM for RCP, as seen in Figure S2.

We next perform numerical analysis of the CD dependence on various parameters. In Figure 4a, we fix the following

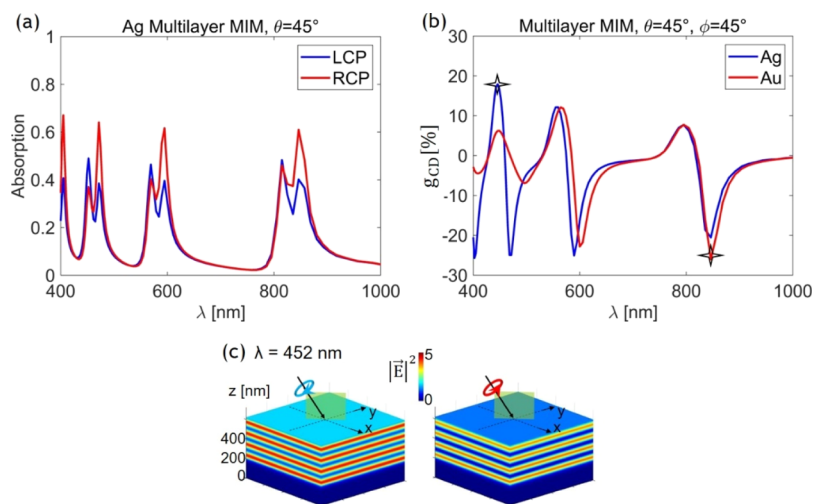


Figure 3. (a) Absorption spectra for the previously investigated multilayer MIM with Ag, excited by LCP or RCP at $\theta = 45^\circ$ and $\phi = 45^\circ$. (b) CD of the multilayer MIM with Ag or Au; stars show the characteristic wavelength points for the electric field visualization. (c) Electric field intensity distribution under oblique LCP and RCP excitation for (c) Ag-based MIM at 452 nm.

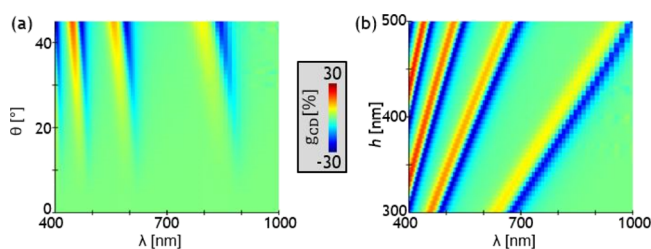


Figure 4. Ag-based MIM CD dependence on various parameters: (a) λ - θ g_{CD} map for $b = 200$ nm, $h = 400$ nm, $t = 20$ nm, and $\phi = 45^\circ$. (b) λ - h g_{CD} map for $b = 200$ nm, $t = 20$ nm, at $\theta = 45^\circ$, and $\phi = 45^\circ$. The two maps have equal color bars.

parameters of Ag-based MIM to $b = 200$ nm, $h = 400$ nm, $t = 20$ nm, and $\phi = 45^\circ$, and we change θ . We see that g_{CD} vanishes at low incidence angles and experiences a blue shift as the incidence angle increases. This is, again, an expected behavior for the FP features, which naturally occur for LCP and RCP excitation, and hence for the resulting CD. Furthermore, the spectral appearance of the FP features directly depends on the insulator α -MoO₃ thickness h ; in Figure 4b, we fix $b = 200$ nm, $t = 20$ nm, $\theta = 45^\circ$, and $\phi = 45^\circ$ and we change h . The enhanced g_{CD} signal can be positioned in the spectral range of interest by properly choosing h ; for example, the highest g_{CD} in the blue range can be obtained in the Ag-based MIM even at lower thicknesses. In ref 43, orthogonal linear polarizations produced different λ - h transmission maps, further proposed for color filters. Here, instead, thickness tuneability at oblique incidence leads to an interesting resonant extrinsic chiral behavior.

Once the geometric parameters of the sample are fixed, it is desirable to address the robustness and tuneability of CD features with respect to the oblique excitation and in-plane tilt. We next investigate Au-based MIM, with parameters $b = 200$ nm, $h = 400$ nm, $t = 20$ nm, and $\theta = 45^\circ$. In Figure 5a, we show that, for a fixed θ , g_{CD} maximum is robust in terms of λ and small ϕ changes around an angle of 45° . Moreover, it inverts sign for the inversion of ϕ . Finally, we consider the absolute g_{CD} maximum in Au-based MIM from Figure 3b, that is, at 846 nm; we investigate CD dependence on θ and ϕ at this wavelength. The θ - ϕ g_{CD} map in Figure 5b shows that, in this

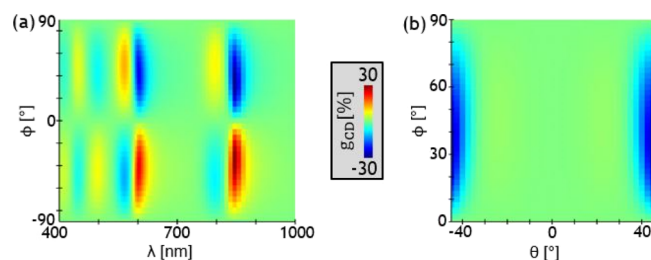


Figure 5. Au-based MIM CD dependence on various parameters: (a) λ - ϕ g_{CD} map for $b = 200$ nm, $h = 400$ nm, and $t = 20$ nm, at $\theta = 45^\circ$ and (b) θ - ϕ g_{CD} map for $b = 200$ nm, $h = 400$ nm, and $t = 20$ nm, at 846 nm. The two maps have equal color bars.

design, g_{CD} can be neither tuned in sign nor increased in the absolute value. Moreover, lowering the incidence angle below 40° leads to a fast decrease in the CD signal.

Moreover, we have tried to optimize the CD behavior in this design at specific wavelengths; we considered 400 nm for the Ag-based MIM as a possible range for the sensing of chiral molecules and laser wavelengths of 633 and 780 nm for the Au-based MIM for the red range. We used a particle swarm algorithm in Lumerical to create a parameter space of the desired parameters to converge to an optimized value of a defined figure of merit.⁴⁵ Top plasmonic thickness was fixed to $t = 20$ nm, as we followed a limit on the minimal film thickness for the continuous Ag layer, compatible with the subsequent α -MoO₃ transfer.⁴³ We then performed the optimization of CD in terms of h , θ , and ϕ . Unfortunately, $|CD|$ was below 30% for all the investigated wavelengths. In the following, we show that the simple, achiral patterning of the top layer yields plasmonic response and leads to much higher CD values, moreover offering wide tuneability.

3.2. Nanostructured MIM. In order to optimize the CD behavior, we address two possible designs, where one of the plasmonic layers is nanostructured with simple, achiral geometry. The proposed pattern is periodic in the xy plane, with periodicity a in both directions. The first design is based on a NHA on a glass substrate. The NHA-MIM design can be obtained with NHA fabrication by focused ion beam milling⁴⁶ or low-cost nanosphere lithography;⁴⁷ the fabrication is then

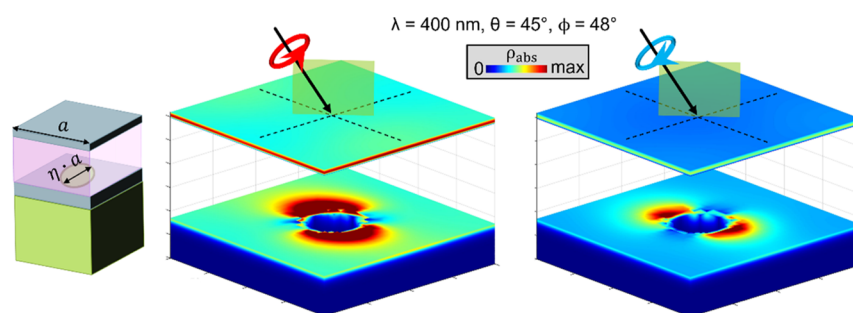


Figure 6. Left inset: schematic of NHA-MIM. The handedness-dependent 3D distribution of the absorption density ρ_{abs} in Ag-based NHA-MIM, optimized at 400 nm.

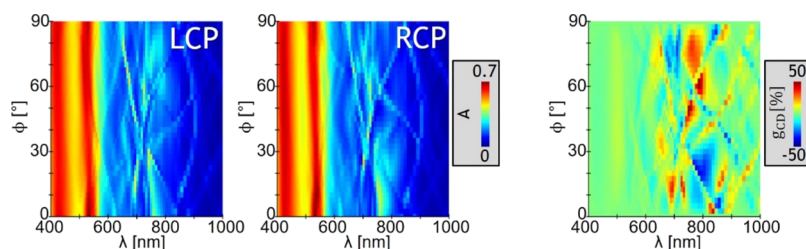


Figure 7. Au-based NHA-MIM, optimized at 780 nm: λ - ϕ maps for LCP and RCP absorption and the corresponding g_{CD} map.

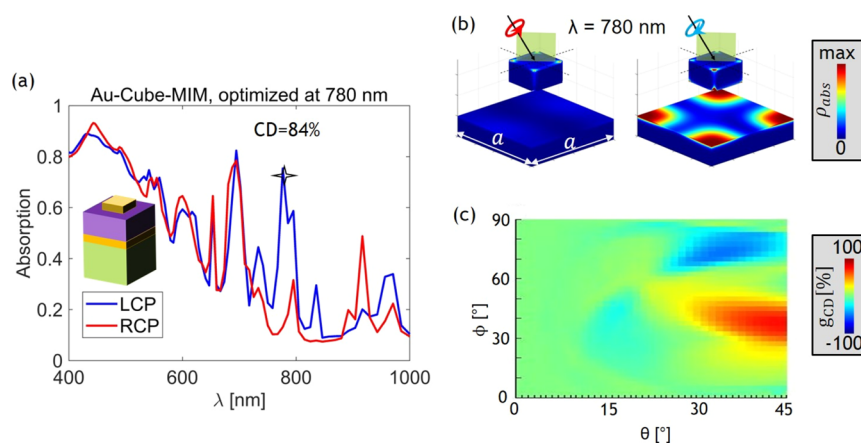


Figure 8. (a) Absorption spectra for the Au-based nanocube MIM, optimized at 780 nm, with CD reaching 84%. (b) Handedness-dependent 3D distribution of the absorption density ρ_{abs} at 780 nm. (c) θ - ϕ g_{CD} map at 780 nm.

followed by α - MoO_3 transfer and a thin-plasmonic layer deposition. The second design considers the patterning of the top layer of the previously presented multilayered structures. This top layer is now a plasmonic nanocube, defining the design as nanocube-MIM.

3.2.1. NHA-MIM. We define a circular nanohole in the bottom plasmonic layer by diameter $D = \eta \cdot a$, where η is a constant in the range from 0.2 to 0.9 (schematic in Figure 6); the constraints are taken to avoid too short diameters or too close NHA rims. Because the nanoholes are circular and the array has the same periodicity in both directions, extrinsic chirality requires both oblique incidence (θ) and the in-plane tilt (ϕ). We first consider the optimization of the parameters a , η , h , θ , and ϕ for Ag-based NHA-MIM exhibiting high g_{CD} at 400 nm. The optimal parameters $a = 200$ nm, $\eta = 0.27$, $h = 400$ nm, $\theta = 45^\circ$, and $\phi = 48^\circ$ improve g_{CD} to 45%. In Figure 6, we plot the 3D absorption density distribution in this optimized sample. RCP excitation leads to stronger confinement of the absorption in the NHA layer. The extrinsic chiral behavior could be measured by scattering-free photo-acoustic technique,

which gives the LCP or RCP total absorption in the metamaterial.⁴⁸

We further optimize Au-based NHA design to a laser wavelength of 780 nm. The parameters $a = 600$ nm, $\eta = 0.9$, $h = 306$ nm, $\theta = 42^\circ$, and $\phi = 61^\circ$ lead to a g_{CD} value of 53%. We next study this behavior to be dependent on wavelength and ϕ , Figure 7. With respect to results for the simple Au-based MIM (Figure 5a), absorption is lower, but the CD behavior rich; it is evident that LCP and RCP light couple to the modes defined by the periodic nature of the metamaterial, being selectively enhanced at specific tilt angles. More importantly, the same sample can be used in the range around 780 nm to obtain opposite CD, by simply rotating the sample with respect to ϕ . Another interesting feature of such metamaterial could be its diffractive behavior in the high energy range, namely, the intensity of the orders diffracted to the glass in such samples strongly depend on the excitation handedness.³⁵ Experimental realization of this design and its diffractive properties would allow us to reach shorter wavelengths (in the blue absorbing range of chiral molecules), and it is the subject of future work.

3.2.2. Nanocube MIM. Plasmonic nanostructures on insulator substrates can greatly enhance electromagnetic field, confine it to subwavelength dimensions, and manipulate its distribution. Moreover, if another metallic layer is put under the thin insulator substrate, near-field coupling between the nanostructure and the metallic layer occurs and a strong magnetic field is formed in the insulator gap. This idea has led to growing interest in a variant of plasmonic resonances known as gap plasmon modes; different combinations of the MIM nanostructuring have been proposed for perfect ultrathin absorbers, metalenses, beam steering, polarization-sensitive scatterers, enhanced photoluminescence, and so forth.^{49–51} Specifically, the simplest gap-plasmon nanoresonator fabrication can be achieved starting from a MIM structure and defining the nanostructure in the top plasmonic layer in a single lithography step.

Next, we add the insulator anisotropy to the subject of gap-plasmon resonances in nanostructures. We consider the Au-based multilayer MIM structure presented before as a starting point; the top Au is then nanostructured to a cube of side $L = \eta \cdot a$. The previous thin layer ($t = 20$ nm) of metal must be now increased in thickness to excite substantial MIM response. Hence, we add parameter t in the optimization at 780 nm. The result of the parameter optimization at this wavelength gives the following parameters: $a = 405$ nm, $t = 200$ nm, $h = 350$ nm, $\eta = 0.37$, $\theta = 45^\circ$, and $\phi = 39^\circ$. The absorption spectra for these parameters are shown in Figure 8a; they are now more complex, showing multiple resonances, while the metasurface resonance for LCP excitation around 780 nm leads to g_{CD} as high as 84%. Very high absorption for this excitation suggests the existence of the gap-plasmon mode; indeed, magnetic field is tightly confined in the α -MoO₃ part below the nanocube in both xz - and yz -planes, Figures S3 and S4. Electric field intensity also suggests coupling of the Au nanocube with the continuous bottom layer for LCP polarization; RCP, instead, is not efficiently coupled to this highly absorbing mode, resulting in an increased reflection. We further visualize the absorption density in Figure 8b; the gap-plasmon mode is efficiently excited for LCP, leading to the drastic absorption increase in the Au bottom layer. We ascribe multiple resonant absorption peaks to various resonance splitting due to the α -MoO₃ anisotropy in the MIM structure, as seen before in the simpler geometry. However, in this design, only g_{CD} at 780 nm is optimized, whereas the same extrinsic chirality conditions lead to less effective chiro-optical control at other wavelengths. This can be appreciated from magnetic field confinement differences for LCP and RCP excitation at other interesting wavelengths: Figure S5 shows that under the conditions optimized for 780 nm, at 695 nm, the nanostructure exhibits another absorption peak; however, this peak is almost equal in intensity for LCP and RCP. At longer wavelength (917 nm), the absorption is lowered, but RCP strongly confines magnetic field close to the bottom Au layer, therefore leading to negative g_{CD} . In principle, one can optimize g_{CD} at any desired wavelength; in Supporting Information, we propose dimensions of Ag-based nanocube MIM and Au-based nanocube MIM at wavelengths 400, 532, 633, and 780 nm, Tables S1 and S2. As expected, the optimized g_{CD} value decreases as the plasmonic properties of metals deteriorate toward smaller wavelengths.

Moreover, this design exhibits interesting tuning features; in Figure 8c, we investigate the θ – ϕ behavior at 780 nm. We notice that, as in the NHA-MIM design, proper orientation of

the sample can produce high g_{CD} signals of both signs. This is an important feature of achiral nanostructures used in extrinsic chirality setups; one sample can provide chiral signals of both signs, and thus, it can be potentially used with both enantiomers. Finally, with respect to Figure 5b, this design allows CD signals starting from much lower angles of incidence.

4. CONCLUSIONS

In conclusion, we have proposed a combination of simple multilayer MIM structures at the nanoscale with biaxial α -MoO₃ as an insulator layer for extrinsic chirality in the visible range. FP resonances of our design are controlled by the material anisotropy and the oblique excitation; their intensity strongly depends on the excitation handedness, leading to a circular dichroic behavior. CD dissymmetry factor g_{CD} of the simplest, planar, multilayered MIM design is below 30% in the visible range. We further show that a simple, achiral nanostructuring of one plasmonic layer can lead to higher g_{CD} and its tunability. The highest g_{CD} for Au-based nanocube MIM structure reaches 84% at 780 nm, arising from the handedness-dependent excitation of gap-surface plasmon resonance. We strongly believe that this idea could lead to new perspectives of α -MoO₃ for various applications based on chiro-optical control and manipulation in the visible range.

■ ASSOCIATED CONTENT

Supporting Information

The Supporting Information is available free of charge at <https://pubs.acs.org/doi/10.1021/acsnm.2c00565>.

Dynamic simulations of complex electric field, handedness-dependent electromagnetic confinement in Au-based MIM at 846 nm, handedness-dependent electromagnetic confinement in Au-based nanocube MIM, and optimized parameters of Ag- and Au-based nanocube MIM at different wavelengths (PDF)

■ AUTHOR INFORMATION

Corresponding Authors

Emilija Petronijevic – Department S.B.A.I., Sapienza Università di Roma, I-00161 Rome, Italy; orcid.org/0000-0003-1034-3843; Email: emilija.petronijevic@uniroma1.it

Koray Aydin – Department of Electrical and Computer Engineering, Northwestern University^{RINGGOLD}, Evanston, Illinois 60208, United States; orcid.org/0000-0002-3268-2216; Email: aydin@northwestern.edu

Authors

Sina Abedini Dereshgi – Department of Electrical and Computer Engineering, Northwestern University^{RINGGOLD}, Evanston, Illinois 60208, United States; orcid.org/0000-0003-2929-0817

Maria Cristina Larciprete – Department S.B.A.I., Sapienza Università di Roma, I-00161 Rome, Italy; orcid.org/0000-0002-7876-628X

Marco Centini – Department S.B.A.I., Sapienza Università di Roma, I-00161 Rome, Italy

Concita Sibilìa – Department S.B.A.I., Sapienza Università di Roma, I-00161 Rome, Italy

Complete contact information is available at: <https://pubs.acs.org/doi/10.1021/acsnm.2c00565>

Author Contributions

The article was written through contributions of all authors. All authors have given approval to the final version of the article.

Notes

The authors declare no competing financial interest.

ACKNOWLEDGMENTS

K.A. acknowledges support from the Air Force Office of Scientific Research under award number FA9550-17-1-0348. K.A. and M.C.L. acknowledge partial support from University La Sapienza for the Visiting Professor Program 2021 (Bando Professori Visitatori 2021).

ABBREVIATIONS

CD, circular dichroism

LCP, left circular polarization

RCP, right circular polarization

REFERENCES

- (1) Nguyen, L. A.; He, H.; Pham-Huy, C. Chiral drugs: An overview. *Int. J. Biomed. Sci.* **2006**, *2*, 85–100.
- (2) Smith, S. W. Chiral Toxicology: It's the Same Thing—Only Different. *Toxicol. Sci.* **2009**, *110*, 4–30.
- (3) Valev, V. K.; Baumberg, J. J.; Sibilia, C.; Verbiest, T. Chirality and chiroptical effects in plasmonic nanostructures: Fundamentals, recent progress, and outlook. *Adv. Mater.* **2013**, *25*, 2517.
- (4) Hentschel, M.; Schäferling, M.; Duan, X.; Giessen, H.; Liu, N. Chiral plasmonics. *Sci. Adv.* **2017**, *3*, No. e1602735.
- (5) Passaseo, A.; Esposito, M.; Cuscunà, M.; Tasco, V. Materials and 3D designs of helix nanostructures for chirality at optical frequencies. *Adv. Opt. Mater.* **2017**, *5*, 1601079.
- (6) Collins, J. T.; Kuppe, C.; Hooper, D. C.; Sibilia, C.; Centini, M.; Valev, V. K. Chirality and Chiroptical Effects in Metal Nanostructures: Fundamentals and Current Trends. *Adv. Opt. Mater.* **2017**, *5*, 1700182.
- (7) Kong, X. T.; Besteiro, L. V.; Wang, Z.; Govorov, A. O. Plasmonic chirality and circular dichroism in bioassembled and nonbiological systems: Theoretical background and recent progress. *Adv. Mater.* **2020**, *32*, 1801790.
- (8) Goerlitzer, E. S. A.; Puri, A. S.; Moses, J. J.; Poulidakos, L. V.; Vogel, N. The Beginner's Guide to Chiral Plasmonics: Mostly Harmless Theory and the Design of Large-Area Substrates. *Adv. Opt. Mater.* **2021**, *9*, 2100378.
- (9) Caridad, J. M.; Tserkezis, C.; Santos, J. E.; Plochocka, P.; Venkatesan, M.; Coey, J. M. D.; Mortensen, N. A.; Rikken, G. L. J. A.; Krstić, V. Detection of the Faraday Chiral Anisotropy. *Phys. Rev. Lett.* **2021**, *126*, 177401.
- (10) Gilroy, C.; Koyroytsaltis-McQuire, D. J. P.; Gadegaard, N.; Karimullah, A. S.; Kadodwala, M. Superchiral hot-spots in "real" chiral plasmonic structures. *Mater. Adv.* **2022**, *3*, 346–354.
- (11) Zhu, A. Y.; Chen, W. T.; Zaidi, A.; Huang, Y.-W.; Khorasaninejad, M.; Sanjeev, V.; Qiu, C.-W.; Capasso, F. Giant intrinsic chiro-optical activity in planar dielectric nanostructures. *Light: Sci. Appl.* **2018**, *7*, 17158.
- (12) Gorkunov, M. V.; Rogov, O. Y.; Kondratov, A. V.; Artemov, V. V.; Gainutdinov, R. V.; Ezhov, A. A. Chiral visible light metasurface patterned in monocrystalline silicon by focused ion beam. *Sci. Rep.* **2018**, *8*, 11623.
- (13) Zanutto, S.; Tredicucci, A.; Navarro-Urrios, D.; Cecchini, M.; Biasiol, G.; Mencarelli, D.; Pierantoni, L.; Pitanti, A. Optomechanics of Chiral Dielectric Metasurfaces. *Adv. Opt. Mater.* **2020**, *8*, 1901507.
- (14) Liao, W.-C.; Liao, S.-W.; Chen, K.-J.; Hsiao, Y.-H.; Chang, S.-W.; Kuo, H.-C.; Shih, M.-H. Optimized spiral metal-gallium-nitride nanowire cavity for ultra-high circular dichroism ultraviolet lasing at room temperature. *Sci. Rep.* **2016**, *6*, 26578.
- (15) Fu, T.; Qu, Y.; Wang, T.; Wang, G.; Wang, Y.; Li, H.; Li, J.; Wang, L.; Zhang, Z. Tunable Chiroptical Response of Chiral Plasmonic Nanostructures Fabricated with Chiral Templates through Oblique Angle Deposition. *J. Phys. Chem. C* **2017**, *121*, 1299–1304.
- (16) Goerlitzer, E. S. A.; Mohammadi, R.; Nechayev, S.; Banzer, P.; Vogel, N. Large-Area 3D Plasmonic Crescents with Tunable Chirality. *Adv. Opt. Mater.* **2019**, *7*, 1801770.
- (17) Kan, Y.; Andersen, S. K. H.; Ding, F.; Kumar, S.; Zhao, C.; Bozhevolnyi, S. I. Metasurface-Enabled Generation of Circularly Polarized Single Photons. *Adv. Mater.* **2020**, *32*, 1907832.
- (18) Palermo, G.; Lio, G. E.; Esposito, M.; Ricciardi, L.; Manoccio, M.; Tasco, V.; Passaseo, A.; De Luca, A.; Strangi, G. Biomolecular Sensing at the Interface between Chiral Metasurfaces and Hyperbolic Metamaterials. *ACS Appl. Mater. Interfaces* **2020**, *12*, 30181–30188.
- (19) Zhao, Y.; Askarpour, A. N.; Sun, L.; Shi, J.; Li, X.; Alù, A. Chirality detection of enantiomers using twisted optical metamaterials. *Nat. Commun.* **2017**, *8*, 14180.
- (20) Solomon, M. L.; Abendroth, J. M.; Poulidakos, L. V.; Hu, J.; Dionne, J. A. Fluorescence-Detected Circular Dichroism of a Chiral Molecular Monolayer with Dielectric Metasurfaces. *J. Am. Chem. Soc.* **2020**, *142*, 18304–18309.
- (21) Lu, X.; Wu, J.; Zhu, Q.; Zhao, J.; Wang, Q.; Zhan, L.; Ni, W. Circular dichroism from single plasmonic nanostructures with extrinsic chirality. *Nanoscale* **2014**, *6*, 14244–14253.
- (22) Plum, E.; Fedotov, V. A.; Zheludev, N. I. Optical activity in extrinsically chiral metamaterial. *Appl. Phys. Lett.* **2008**, *93*, 191911.
- (23) Plum, E.; Liu, X.-X.; Fedotov, V. A.; Chen, Y.; Tsai, D. P.; Zheludev, N. I. Metamaterials: Optical Activity Without Chirality. *Phys. Rev. Lett.* **2009**, *102*, 113902.
- (24) Yannopapas, V. Circular dichroism in planar nonchiral plasmonic metamaterials. *Opt. Lett.* **2009**, *34*, 632–634.
- (25) De Leon, I.; Horton, M. J.; Schulz, S. A.; Upham, J.; Banzer, P.; Boyd, R. W. Strong, spectrally-tunable chirality in diffractive metasurfaces. *Sci. Rep.* **2015**, *5*, 13034.
- (26) Mao, L.; Liu, K.; Zhang, S.; Cao, T. Extrinsically 2D-Chiral Metamirror in Near-Infrared Region. *ACS Photonics* **2020**, *7*, 375–383.
- (27) Nemiroski, A.; Gonidec, M.; Fox, J. M.; Jean-Remy, P.; Turnage, E.; Whitesides, G. M. Engineering Shadows to Fabricate Optical Metasurfaces. *ACS Nano* **2014**, *8*, 11061–11070.
- (28) Belardini, A.; Larciprete, M. C.; Centini, M.; Fazio, E.; Sibilia, C.; Chiappe, D.; Martella, C.; Toma, A.; Giordano, M.; Buatier De Mongeot, F. Circular Dichroism in the Optical Second-Harmonic Emission of Curved Gold Metal Nanowires. *Phys. Rev. Lett.* **2011**, *107*, 257401.
- (29) Leahu, G.; Petronijevic, E.; Belardini, A.; Centini, M.; Sibilia, C.; Hakkarainen, T.; Koivusalo, E.; Rizzo Piton, M.; Suomalainen, S.; Guina, M. Evidence of optical circular dichroism in GaAs-based nanowires partially covered with gold. *Adv. Opt. Mater.* **2017**, *5*, 1601063.
- (30) Wang, Y.; Qi, J.; Pan, C.; Wu, Q.; Yao, J.; Chen, Z.; Chen, J.; Li, Y.; Yu, X.; Sun, Q.; Xu, J. Giant circular dichroism of large-area extrinsic chiral metal nanorecents. *Sci. Rep.* **2018**, *8*, 3351.
- (31) Hakkarainen, T.; Petronijevic, E.; Rizzo Piton, M.; Sibilia, C. Demonstration of extrinsic chirality of photoluminescence with semiconductor-metal hybrid nanowires. *Sci. Rep.* **2019**, *9*, 5040.
- (32) Goerlitzer, E. S. A.; Mohammadi, R.; Nechayev, S.; Volk, K.; Rey, M.; Banzer, P.; Karg, M.; Vogel, N. Chiral surface lattice resonances. *Adv. Mater.* **2020**, *32*, 2001330.
- (33) Petronijevic, E.; Belardini, A.; Cesca, T.; Scian, C.; Mattei, G.; Sibilia, C. Rich near-infrared chiral behavior in diffractive metasurfaces. *Phys. Rev. Appl.* **2021**, *16*, 014003.
- (34) Petronijevic, E.; Belardini, A.; Leahu, G.; Hakkarainen, T.; Piton, M. R.; Koivusalo, E.; Sibilia, C. Broadband optical spin dependent reflection in self-assembled GaAs-based nanowires asymmetrically hybridized with Au. *Sci. Rep.* **2021**, *11*, 4316.
- (35) Leahu, G.; Petronijevic, E.; Li Voti, R.; Belardini, A.; Cesca, T.; Mattei, G.; Sibilia, C. Diffracted Beams from Metasurfaces: High Chiral Detectivity by Photothermal Deflection Technique. *Adv. Opt. Mater.* **2021**, *9*, 2100670.

- (36) Wu, X.; Fu, C.; Zhang, Z. M. Chiral response of a twisted bilayer of hexagonal boron nitride. *Opt. Commun.* **2019**, *452*, 124–129.
- (37) Liu, Z.; Aydin, K. Localized Surface Plasmons in Nanostructured Monolayer Black Phosphorus. *Nano Lett.* **2016**, *16*, 3457–3462.
- (38) Hong, Q.; Xu, W.; Zhang, J.; Zhu, Z.; Yuan, X.; Qin, S. Optical activity in monolayer black phosphorus due to extrinsic chirality. *Opt. Lett.* **2019**, *44*, 1774–1777.
- (39) Matthaikakakis, N.; Droulias, S.; Kakarantzas, G. Dynamic Control of Light Chirality with Nanostructured Monolayer Black Phosphorus for Broadband Terahertz Applications. *Adv. Opt. Mater.* **2022**, *10*, 2102273.
- (40) Abedini Dereshgi, S.; Folland, T. G.; Murthy, A. A.; Song, X.; Tanriover, I.; Dravid, V. P.; Caldwell, J. D.; Aydin, K. Lithography-free IR polarization converters via orthogonal in-plane phonons in α -MoO₃ flakes. *Nat. Commun.* **2020**, *11*, 5771.
- (41) Abedini Dereshgi, S.; Larciprete, M. C.; Centini, M.; Murthy, A. A.; Tang, K.; Wu, J.; Dravid, V. P.; Aydin, K. Tuning of Optical Phonons in α -MoO₃-VO₂ Multilayers. *ACS Appl. Mater. Interfaces* **2021**, *13*, 48981–48987.
- (42) Wu, B.; Wang, M.; Wu, F.; Wu, X. Strong extrinsic chirality in biaxial hyperbolic material α -MoO₃ with in-plane anisotropy. *Appl. Opt.* **2021**, *60*, 4599–4605.
- (43) Wei, C.; Abedini Dereshgi, S.; Song, X.; Murthy, A.; Dravid, V. P.; Cao, T.; Aydin, K. Polarization Reflector/Color Filter at Visible Frequencies via Anisotropic α -MoO₃. *Adv. Opt. Mater.* **2020**, *8*, 2000088.
- (44) Lumerical Solutions, Inc. <http://www.lumerical.com/tcad-products/fdtd/> (last accessed on March 22, 2022).
- (45) Petronijevic, E.; Sibilija, C. All-optical tuning of EIT-like dielectric metasurfaces by means of chalcogenide phase change materials. *Opt. Express* **2016**, *24*, 30411–30420.
- (46) Chen, Y.; Bi, K.; Wang, Q.; Zheng, M.; Liu, Q.; Han, Y.; Yang, J.; Chang, S.; Zhang, G.; Duan, H. Rapid Focused Ion Beam Milling Based Fabrication of Plasmonic Nanoparticles and Assemblies via “Sketch and Peel” Strategy. *ACS Nano* **2016**, *10*, 11228–11236.
- (47) Petronijevic, E.; Belardini, A.; Leahu, G.; Cesca, T.; Scian, C.; Mattei, G.; Sibilija, C. Circular dichroism in low-cost plasmonics: 2D arrays of nanoholes in silver. *Appl. Sci.* **2020**, *10*, 1316.
- (48) Petronijevic, E.; Leahu, G.; Li Voti, R.; Belardini, A.; Scian, C.; Michieli, N.; Cesca, T.; Mattei, G.; Sibilija, C. Photo-acoustic detection of chirality in metal-polystyrene metasurfaces. *Appl. Phys. Lett.* **2019**, *114*, 053101.
- (49) Ding, F.; Yang, Y.; Deshpande, R. A.; Bozhevolnyi, S. I. A review of gap-surface plasmon metasurfaces: fundamentals and applications. *Nanophotonics* **2018**, *7*, 1129–1156.
- (50) Pors, A.; Bozhevolnyi, S. I. Plasmonic metasurfaces for efficient phase control in reflection. *Opt. Express* **2013**, *21*, 27438–27451.
- (51) Petronijevic, E.; Centini, M.; Cesca, T.; Mattei, G.; Bovino, F. A.; Sibilija, C. Control of Au nanoantenna emission enhancement of magnetic dipolar emitters by means of VO₂ phase change layers. *Opt. Express* **2019**, *27*, 24260.